

# Layered structure of alumina/graphene-augmented-inorganic-nanofibers with directional electrical conductivity

Ali Saffar Shamshirgar<sup>a</sup>, Rocio Estefania Rojas Hernández<sup>a</sup>, Girish C. Tewari<sup>b</sup>, Roman Ivanov<sup>a</sup>, Valdek Mikli<sup>c</sup>, Maarit Karppinen<sup>b</sup>, Irina Hussainova<sup>a,\*</sup>

<sup>a</sup> Department of Mechanical and Industrial Engineering, Tallinn University of Technology, Ehitajate tee 5, 19086, Estonia

<sup>b</sup> Department of Chemistry and Materials Science, Aalto University, P.O. Box 16100, FI-00076, Aalto, Finland

<sup>c</sup> Laboratory of Optoelectronic Materials Physics, Department of Material and Environmental Technology, Tallinn University of Technology, Ehitajate tee 5, 19086, Estonia

## ARTICLE INFO

### Article history:

Received 13 December 2019

Received in revised form

25 April 2020

Accepted 12 June 2020

Available online 20 June 2020

### Keywords:

Hierarchical structures

Hybrid materials

Ceramics

Graphene

Anisotropy

## ABSTRACT

Implementation of layered structures with strong nanoscale optimized interfaces, enables engineering of materials with functional properties. In this work, anisotropic functional multi-layered structures are produced by integration of a thin hybrid inter-layer of graphene-augmented-nanofibers/alumina into  $\alpha$ -alumina through an ex-situ strategy of precipitating the tailored hybrid from a solution. Spark plasma sintering was used to consolidate the layered structures at 1150 and 1450 °C under 75 and 50 MPa pressure. Raman spectroscopy suggests presence of C–H bonds and  $sp^3$  hybridization for the samples sintered at 1150 °C, while graphene structure is purified at the sintering temperature of 1450 °C. The multilayer structures demonstrate a high in-plane electrical conductivity which can be modulated, ranging from 300 to 1800 S m<sup>-1</sup> as a function of the interlayer thickness and the carbon content. A p-type conduction at room temperature and n-type down to 4 K in graphene-augmented nano-fillers was observed in Hall measurement. However, the multilayered systems display a p-type conduction in the entire temperature range. Hardness was preserved despite the high concentration of the graphene-augmented nano-fillers in the hybrid interlayer leaving a highest value of ~22 GPa. The results have the potential to fuel the development of functional electronic enclosures with additional functionalities such as electromagnetic interference shielding.

© 2020 Elsevier Ltd. All rights reserved.

## 1. Introduction

The technological development continuously imposes strong requirements for engineering materials with improved mechanical reliability and additional functionalities. To address this challenge, even widely used materials should demonstrate unprecedented combination of several, and sometimes mutually exclusive, properties. Ceramic materials, such as alumina (Al<sub>2</sub>O<sub>3</sub>), boron carbide (B<sub>4</sub>C) and silicon carbide (SiC), are some of the most widely used ceramics for many industrial applications due to lightweight, high compressive strength, thermal stability and oxidation/corrosion resistance. However, brittle fracture behavior often limits reliability of these ceramics. A rational solution to this problem can be found in the Nature, which provides a rich source of inspiration by

locating specific compositions and architectures in assigned regions, generating multiple advantages within a bulk material. One of the examples is the layered structures that mimic the micro-structure of nacre and abalone shell, which are widely employed to improve toughness of otherwise brittle materials [1,2].

Biological materials can exhibit remarkable combinations of stiffness, strength, toughness, and low density, which are in some cases unmatched by synthetic materials [3]. However, through the incorporation of architected structures (i.e. multilayer, core-shell, etc.), some of these nature-developed structures can be technologically designed to meet versatile requirements and enhance functional performance. For instance, to increase mechanical efficiency, general design principle is the combination of stiff and relatively strong exterior with a weaker interior; for synthetic materials, layered architecture enables increase in fracture toughness through introduction of numerous interfaces. Many natural materials have evolved even some steps further to envisage addition of non-mechanical functions such as the structure of skin

\* Corresponding author.

E-mail addresses: [irina.hussainova@taltech.ee](mailto:irina.hussainova@taltech.ee), [irhus@staff.ttu.ee](mailto:irhus@staff.ttu.ee) (I. Hussainova).

which contains perspiration glands, sensory receptors, hair follicles, and blood vessels, together with basic functionality as a protecting layer. Similarly, in synthetic materials, addition of new functionalities such as an electro-conductive layer may allow for a directional materials response, i.e. high anisotropy in thermal and electrical conduction which opens venues for diverse applications including heat management [4], electro calorific effect [5], electromagnetic interference (EMI) shielding [6], multilayer ceramic capacitors, etc. Correspondingly, a wide variety of reinforcing and/or toughening additives such as fibers, carbon nanotubes and, recently, graphene nano-platelets, have been incorporated into ceramic matrices to increase damage tolerance of the final product [7,8]. These fillers can influence not only toughness but also give specific functionality to the material. Recently, graphene reinforced ceramics have attracted an unprecedented attention because of the extraordinary properties of graphene [9] combined with the inhibition of grain growth during sintering and subsequent enhancement in mechanical properties [10–12]. It should be noted that the term “graphene” refers exclusively to the pure monolayer of carbon atoms arranged in a honeycomb type structure [9]; nonetheless, different types of graphene-like structures (graphene nano-platelets, graphene nano-sheets, graphene oxide layers, reduced graphene oxide, etc.) are common for composites’ reinforcement. Experimentally, it has been demonstrated that addition of graphene nanoplatelets to ceramic matrix also can enhance electrical conductivity by orders of magnitudes depending on the concentration of the fillers [12,13]. Similarly, enhanced conductivity of an insulating material such as alumina, by incorporation of nanorods, is shown to be dependent on the concentration and the aspect ratio of the conductive fillers [12,14], which affects the tunneling length and subsequently electrical percolation threshold [13–15]. On the other hand, a vast number of studies have proven that graphene fillers are suitable candidates for a variety of applications such as electromagnetic interference (EMI) shielding. Ru et al. in Ref. [16] achieved EMI shielding effectiveness >32 dB in the K band with less than 1 vol% rGO in a mullite matrix composite. Luo et al. doubled the dielectric constant of BaTiO<sub>3</sub> with 3 wt% addition of graphene nanosheets [17]. Subsequently, as far as additional functionality is concerned, alternating layers of copper/nickel and graphene with ultrahigh strength of 1.5–4 GPa has been reported by Kim et al. [15]. Directional electrical conductivity of  $10^3 \text{ S m}^{-1}$  in alternating layers of Si<sub>3</sub>N<sub>4</sub> and graphene sheets has been demonstrated in Refs. [18]. Remarkable increase in in-plane conductivity as compared to the conductivity measured for the through-thickness direction is reported for Si<sub>3</sub>N<sub>4</sub>/graphene nanoplates [19], and composites of Al<sub>2</sub>O<sub>3</sub>/graphene nanoplates [20].

Nevertheless, high anisotropic electrical conductivity achieved in straightforward assemblies has merits for improvement. In this work, a bottom-up method of hot-wall chemical vapor deposition (CVD) has been used for production of the conductive nano-reinforcements. In this method, thermal decomposition of CH<sub>4</sub> at 1000 °C with hydrogen etching, assembles carbon atoms into polycrystalline graphene layers on the surface of  $\gamma$ -Al<sub>2</sub>O<sub>3</sub> nanofibers that were used as substrate for growing graphene. The developed graphene-augmented alumina nanofibers (GAIN) described in detail elsewhere [8,21] employed in this work, meet electrical percolation threshold in an  $\alpha$ -alumina composite at <3 wt % of the fillers loading (–0.39 wt% of calculated carbon content), and tunneling length of 2.23 nm [8,12,22]. To address the challenge of integrating new functionalities to ceramics together with maintaining or enhancement of their mechanical properties, this work employs the above-mentioned GAIN fillers and focuses on engineering of novel hierarchical ceramic hybrids with alternating layers owning high anisotropy in electrical properties. In this straightforward and cost-effective approach, alternating layers of

$\alpha$ -alumina and alumina/graphene hybrids are constructed directly in the spark plasma sintering (SPS) die through a filtration method, which greatly simplifies the process. Ultimately, the sintered structures represent the integration of multiple gradients, namely, microstructural gradient in terms of grain size, porosity, and subsequently, mechanical properties; and anisotropic electrical properties. The developed structures could be potentially used for the fabrication of impact resistance structures, electrostatic charge dissipators, EMI shielding, or thermoelectric devices.

## 2. Experimental

### 2.1. Materials processing

The commercially available  $\alpha$ -Al<sub>2</sub>O<sub>3</sub> nano-powder with an average particle size of 100 nm (TM-DAR, Taimei, Japan) was used as the matrix material. Graphene augmented inorganic nanofibers (GAIN) were exploited as fillers in the hybrid interlayers. The graphene layers were grown on a surface of highly aligned alumina ( $\gamma$ -Al<sub>2</sub>O<sub>3</sub>) nanofibers [23] along the longitudinal axis by the means of a single step catalyst-free hot-wall CVD technique in a tube furnace kept at 1000 °C for 20 min. Aligned  $\gamma$ -alumina bundles of 4 cm long and  $0.7 \times 0.7$  cm in cross section were prepared having ~0.15 g dry weight as substrate for CVD graphene. (see Supplementary Information, S1).

The ratios of 15 and 25 wt% loading of GAIN and 85–75 wt%  $\alpha$ -Al<sub>2</sub>O<sub>3</sub> nano-powder was weighted corresponding to a consolidated thickness of 100  $\mu\text{m}$  for the interlayer of the samples with 20 mm diameter. A separate sample with 500  $\mu\text{m}$  interlayer thickness was considered to investigate the contribution of thickness to electrical conductivity. The prepared compositions were dispersed in chloroform by a sonication rod (Hielscher UP400S) for 20 min at 30W using alternative regime 4 s ON - 1 s OFF. Two green pellets of  $\alpha$ -Al<sub>2</sub>O<sub>3</sub> nano-powder corresponding to a sintered thickness of 2 mm were produced under 5 MPa of pressure to insert as the top and bottom layers of the structures in the SPS die. The layered structure was implemented exploiting a pseudo-colloidal method, directly in a SPS graphite mold with diameter of 20 mm. A schematic of the sample preparation process is illustrated in Fig. 1a and detailed in Supplementary information, S2. The stacked materials were spark plasma sintered (Dr. Sinter SPS-510CE, Japan) in N<sub>2</sub> atmosphere at two different regimes: (i) 1450 °C with simultaneous 50 MPa uniaxial pressure for a dwell time of 10 min (hereafter abbreviated as high temperature (HT) approach); and (ii) 1150 °C with simultaneous 75 MPa uniaxial pressure for a dwell time of 10 min (hereafter abbreviated as low temperature (LT) approach). The two different regimes were used to understand how the phase evolution and subsequently microstructural features can be influenced by sintering temperature. With a focus on full densification, the HT sintering approach was used guided by a pervious study on spark plasma sintering of alumina [24] and following the procedure explained in detail elsewhere [25]. While, to avoid gamma to alpha phase transition in GAIN fibers, the experimental parameters of LT sintering approach were chosen guided by a pervious report on sintering of transparent alumina [26]. Table 1 provides full data-sheet of the samples’ compositions and sintering conditions. The heating rate was set to 200 °C/min between 600 and 1000 °C and then 100 °C/min. Moreover, to portrait versatility of the proposed pseudo-colloidal approach for implementing layered structures, a sample with three interlayers is manufactured in A-B-A-B-A fashion in which A stands for alumina layer and B stands for 25 wt% GAIN composite layers. All interlayers have similar thickness of  $100 \pm 10 \mu\text{m}$  (see Supplementary information, S3).

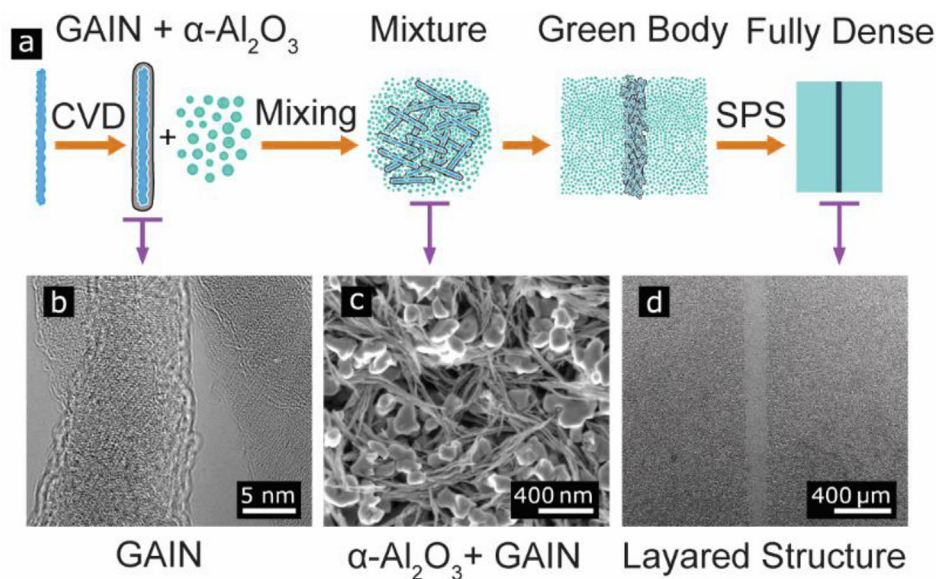


**Fig. 1.** (a) Schematic of the manufacturing steps to produce the layered structures, (b) TEM micrograph of the graphene-augmented  $\gamma\text{-Al}_2\text{O}_3$  nanofibers, (c) SEM micrograph of the GAIN/ $\alpha\text{-Al}_2\text{O}_3$  dried suspension, (d) SEM of the hybrid interlayer sandwiched between layers of  $\text{Al}_2\text{O}_3$  after SPS (sample 15%-HT). (A colour version of this figure can be viewed online.)

**Table 1**  
Index of the samples and process parameters.

Designation	Sintering temperature( $^{\circ}\text{C}$ )	Pressure[MPa]	Hybrid layer thickness[ $\mu\text{m}$ ]	Calculated GAIN <sup>a</sup> [Wt.%]	Calculated Carbon[Wt.%]
15%-HT	1450	50	100	15	~1.95
15%-LT	1150	75	100	15	~1.95
25%-HT	1450	50	100	25	~3.25
25%-LT	1150	75	100	25	~3.25
25%-HT-500	1450	50	500	25	~3.25

<sup>a</sup> Graphene-augmented Inorganic Nanofibers.

## 2.2. Characterization

Carbon content of the CVD graphene augmented alumina nanofibers was determined using a LECO CS 200 carbon-Sulphur analyzer. Three measurements were made, and the arithmetic mean was used to calculate the corresponding carbon content of the composites. Resulting size of the fibers after mixing was determined by laser scattering method using Mastersizer 3000, Malvern Panalytical, equipped with a  $\lambda = 632.8$  nm He–Ne laser.

The samples with final sintered thickness of  $4 \pm 0.1$  mm were polished to  $0.5$   $\mu\text{m}$  surface roughness using diamond disc and diamond suspension. Raman spectra of the as-synthesized multilayered material were recorded using a Horiba's LabRAM 800 high-resolution spectrometer equipped with a 532 nm laser excitation wavelength at room temperature (RT) and a 50X objective lens ( $\text{NA} = 0.95$ ). The incident laser power was 7 mW. Raman spectral resolution of the system was  $1.5$   $\text{cm}^{-1}$ . For microstructural characterization of the fillers and bulks, a field emission scanning electron microscope (FEG-SEM Zeiss ULTRA-55, Germany) equipped with EDS (energy dispersive X-ray spectrometer, BRUKER, Esprit 1.82 system, USA) with voltage of up to 20 kV and magnifications up to 50 kX was used. The grain size analysis was performed by imaging analysis method on SEM images considering at least 500 readings using Image Pro Plus 7.0 package by Media Cybernetics. All the SEM images for this analysis were recorded at the same magnification (5000x) and at least three micrographs of each sample were analyzed to get statistics that are more reliable.

In plane DC electrical resistivity measurements were performed

on the multilayered bars from room temperature to 400 K using a two-probe array. Prior to the measurement in order to prepare electrical probing areas, first, 80 nm Pt was deposited on the sides of the samples using a Cressington 308R coating system. Second, 0.5 mm Ag conductive paste was applied on top of the Pt coatings, and last, samples were thermal treated at  $100$   $^{\circ}\text{C}$  for 12 h in a muffle furnace in air. The low temperature transport properties (electrical resistivity and Hall coefficient) of the GAIN fillers and composites with 15 and 25 wt% of GAIN in alumina matrix were measured using a physical property measurement system (PPMS; Quantum design; equipped with 9 T magnetic field) with Hall bar configuration from 4K to 300K.

Vickers microhardness tests were carried out under 4.9 N load (HV0.5) using BUEHLER MICROMET 2001 equipped with a square-based orthogonal pyramidal diamond indenter on the cross section of the samples in 3 different regions: hybrid interlayer, monolithic alumina layer, and interface between the layers. The load was kept for 10 S for each indent. HV values were estimated from the average values of 10 indents in each region and converted to SI unit using Equation (1) according to Annex F, ISO 14577–1:2015.

$$HV = (H_{IT} \times A_p) / (g \times A_s) = 0.0945 H_{IT} \text{ (GPa)} \quad (1)$$

In this equation, HV is the Vicker's hardness,  $H_{IT}$  indentation hardness,  $A_p$  projected area of the indenter,  $A_s$  contact surface area, and  $g$  is the gravitational acceleration. NanoTest Vantage (Micro-Materials Ltd, UK) nanoindenter equipped with a diamond Berkovich tip was used to perform the nanoindentation tests on well grinded and polished samples following the procedure outlined in



Ref. [27]. The tests were load-controlled and conducted at room temperature. Prior to the test, a calibration was performed on the Berkovich diamond indenter with hardness of 1140 GPa and Poisson's ratio of 0.07 using a standard fused silica specimen. Loading was performed at 10 mN/s with dwell time of 5s and unloading rate of 10 mN/s. The drift rate was preset to <0.05 nm/s before the beginning of each indentation test.

### 3. Results and discussion

#### 3.1. Microstructure

After Processing, the resulting length of the graphenated fibers is measured to be  $\sim 700 \pm 100$  nm. From the FE-SEM micrograph of the alumina/GAIN mixture Fig. 1c homogeneous distribution of the fibers of 30:1 to 40:1 aspect ratio (fibers diameter is  $\sim 20 \pm 5$  nm) is recognizable. A cross section of the layered structure (15%-HT) with the hybrid interlayer sandwiched between two layers of monolithic alumina is shown in Fig. 1d. The presence of conductive fillers enables the local joule heating at elevated temperatures, providing a homogenous thermal distribution and hindering the migration of grain boundaries (GB) during SPS; therefore, a grain refinement in the interlayer, affected by the presence of the fillers is expectedly obtained [12,25]. Although highly resistive alumina powder (top and bottom layers of the multilayer) would prohibit the local joule heating in the early stages of the SPS, as the temperature increases, the resistivity of alumina sharply decreases ( $\sim 10^4 \Omega \text{ m}$  at  $1000^\circ\text{C}$ ) [28,29] providing an electrical discharge path parallel to the SPS axis through the sample. Subsequently, the joule heating phenomenon manifests as local high temperature fields which impact the microstructural evolution [30]. Fig. 2 shows the microstructure and grain size distribution of different layers in the case of 15 wt % GAIN in (a,b,c), and 25 wt % GAIN in (d,e,f) for the samples sintered at  $1450^\circ\text{C}$  under 50 MPa of pressure. Note that the microstructure of the 25%-HT and 25%-HT-500 are identical; therefore, only the micrographs of 25%-HT are chosen for comparison. It was previously mentioned that presence of GAIN impedes grain growth in

the interlayer. However, apart from that, the  $\gamma$ -alumina nature of the substrate nanofibers used for growing graphene grains can be the secondary attributing factor to the grain refinement. In fact, presence of few percentages of  $\gamma$ -alumina in an  $\alpha$  matrix on its own is not an influencing factor, rather the contribution of the  $\gamma$  phase to densification by nucleation and grain growth through the transitional process of  $\gamma \rightarrow \delta \rightarrow \theta \rightarrow \alpha\text{-Al}_2\text{O}_3$  is governing the sintering mechanism. In other words, presence of  $\gamma$  phase reduces the densification temperature to  $1450^\circ\text{C}$  while this process starts in the temperature range of  $1050\text{--}1200^\circ\text{C}$  depending on the particle size of the initial powder. The transition of  $\theta \rightarrow \alpha$  can produce vermicular microstructure that forms a network of wide pores. The resulted porous structure requires temperatures higher than  $1600^\circ\text{C}$  for high densification [31,32]. Presence of the vermicular microstructure is visible in Fig. 2e where the sample was sintered at  $1450^\circ\text{C}$  with heating rate of  $100^\circ\text{C}/\text{min}$ . Controlling the rearrangement of grains during  $\theta \rightarrow \alpha\text{-Al}_2\text{O}_3$  transition by employing a significantly lower heating rate is one possible way to eliminate this structure [32]. However, as an alternative mechanism, the sintering temperature of  $1150^\circ\text{C}$  was chosen in this work to avoid the phase transition of  $\gamma\text{-Al}_2\text{O}_3$  used as CVD substrate to produce GAIN fibers. Supplementary information, S4, provides information on phase transformation of the GAIN at different temperatures. The temperature was chosen based on a previous thermal analysis done by the authors in Ref. [23]. On the other hand, the interlayer also contributes to the grain structure of the monolithic alumina layers. It is visible from Fig. 2a,d that average grain size in monolithic alumina is  $\sim 5 \mu\text{m}$  in the case of samples with 15 wt % GAIN interlayer. This is while, in the case of the sample with 25 wt % GAIN comparatively a slight grain refinement in the monolithic alumina layer is achieved with average grain size of  $\sim 2 \mu\text{m}$ . Additional SEM micrographs are presented in Fig. S5 for comparison of grain size of the monolithic alumina layers (see Supplementary information, S5). This can be attributed to a better heat distribution in the SPS die during the sintering, benefiting from a larger fibrous conductive filler content present in the interlayer. Nevertheless, the grain structure in the monolithic alumina is greatly larger as compared to

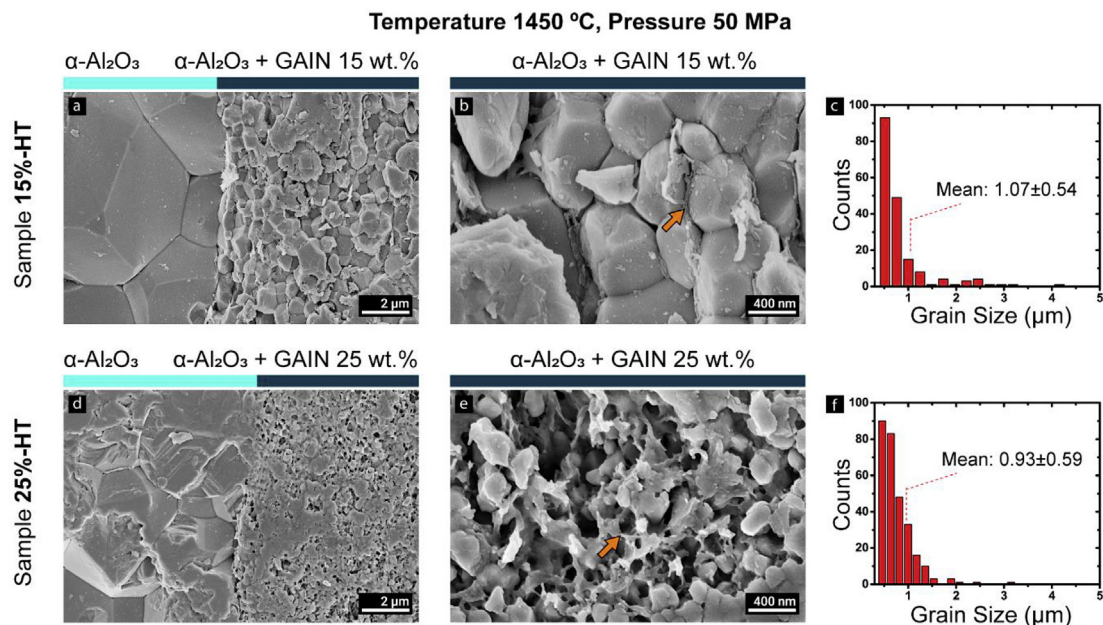


**Fig. 2.** SEM micrograph of SPS samples sintered at  $1450^\circ\text{C}$  under 50 MPa; (a,d) interface between the hybrid layer and monolithic  $\alpha\text{-Al}_2\text{O}_3$ , (b,e) interlayer in the sample with 15 and 25 wt % GAIN respectively - arrows pointing at GAIN fibers in the microstructure, (c,f) interlayer grain size distribution in samples with 15 and 25 wt % GAIN, respectively. (A colour version of this figure can be viewed online.)

the grains of hybrid interlayers. As a result, a sharp interface between the  $\text{Al}_2\text{O}_3$  and interlayer has formed Fig. 2a,d. Fig. 3 displays the microstructure and grain size distribution of the layers in the case of 15 wt % GAIN in (a,b,c), and 25 wt % GAIN in (d,e,f) for the samples sintered at 1150 °C under 75 MPa of pressure. As demonstrated in Fig. 2b,e and Fig. 3b,e presence of 25 wt % GAIN which roughly is equal to a calculated 3.25 wt% of carbon content, results in a refined structure interlayer by hindering the migration of GB during sintering, independent of the sintering temperature. The arithmetic mean of carbon content in the GAIN fibers shows a value of 13 wt % which was used to determine the weight percentage of carbon in the hybrid interlayer of the layered structures. Although grains in the 25 wt % GAIN hybrid interlayer are much smaller than those in 15 wt % GAIN, the level of residual porosity seems to be much higher due to the presence of larger carbon content and its corresponding negative effect on the densification [33,34]. The  $\text{Al}_2\text{O}_3$  grain refinement at low sintering temperature (1150 °C) generates a less coarse grain structure with much smaller grains in the monolithic layers. Subsequently, no interface is visible between the interlayer and the monolithic  $\text{Al}_2\text{O}_3$  in the samples sintered at low temperature.

The yellow vertical lines in Fig. 3a,d shows the location of the interface that is visible only at low magnifications. Additional SEM images together with Raman spectroscopy graphs are presented in Supplementary information, S6, for further visualization of the locations of the interlayers and their corresponding compositions. The grains of the monolithic alumina in the case of 1150 °C sintering temperature have average sizes of 400 and 300 nm for samples with 15 wt % GAIN and 25 wt % GAIN hybrid interlayers respectively estimated from 10 readings in FE-SEM micrographs.

The pre-processing of the FE-SEM micrographs for determination of the grain size distribution includes usual steps of median filter and thresholding. However, unlike the monolithic grain structure, the grains in the interlayer could not be separated only by thresholding due to the presence of fibrous nano fillers, which form flaky layers at the GB areas. To overcome the issue, an additional watershed filter was applied. The filter successfully separated the

grains; however, the process uncertainty consists of occasional fragmented detection of the grains by the software. Hence, the absolute values of the results should not be taken as the actual grain size. Nonetheless, as all the images were processed and analyzed under the same steps, the results represent relatively realistic determinations for comparing the interlayers in the samples. As shown in Fig. 2c,f and Fig. 3c,f the grain size distribution is significantly narrower in the case of the low temperature sintering. The lower fraction of GAIN in 15%-LT results in a flatter distribution graph as compared to 25%-LT. Moreover, a larger population of finer grains are present in the samples with 15 wt% GAIN.

### 3.2. Mechanical properties

Three different regions were chosen to study the effect of the sintering conditions and the GAIN fraction on the mechanical properties of the multilayer structures. Micro-hardness indentations were introduced into the monolithic alumina, hybrid layer, and the interface between the layers. An optical image of the intended areas is shown in Fig. 4a; and Vicker's hardness (HV) values and nanoindentation data are summarized in Table 2. The values obtained for monolithic alumina are in a good agreement with the results obtained for fully dense alumina prepared by high pressure hot press, hot isostatic press or SPS techniques [35]. Nearly similar values were obtained for the samples 15%-HT, 15%-LT, and 25%-HT in three sections. However, in the case of the sample 25%-LT, the HV decreases down to 11.3 GPa as a result of high porosity at the interface and the hybrid layer. Amongst the samples, 15%-LT reveals the highest hardness values, in which the hybrid layer hardness of 22.2 GPa is comparable to hardness of monolithic alumina. This fact is conditioned by the combined effect of grain refinement and low level of porosity. A slight distortion in the indent shape seen in Fig. 4b can be explained by structural anisotropy. This anisotropy is developed due to two factors: (i) pressure-induced preferential grain growth during the SPS; and (ii) interaction of the DC field with the electrostatic charges of the GBs. In the vicinity of interlayer, the preferred orientation induced by

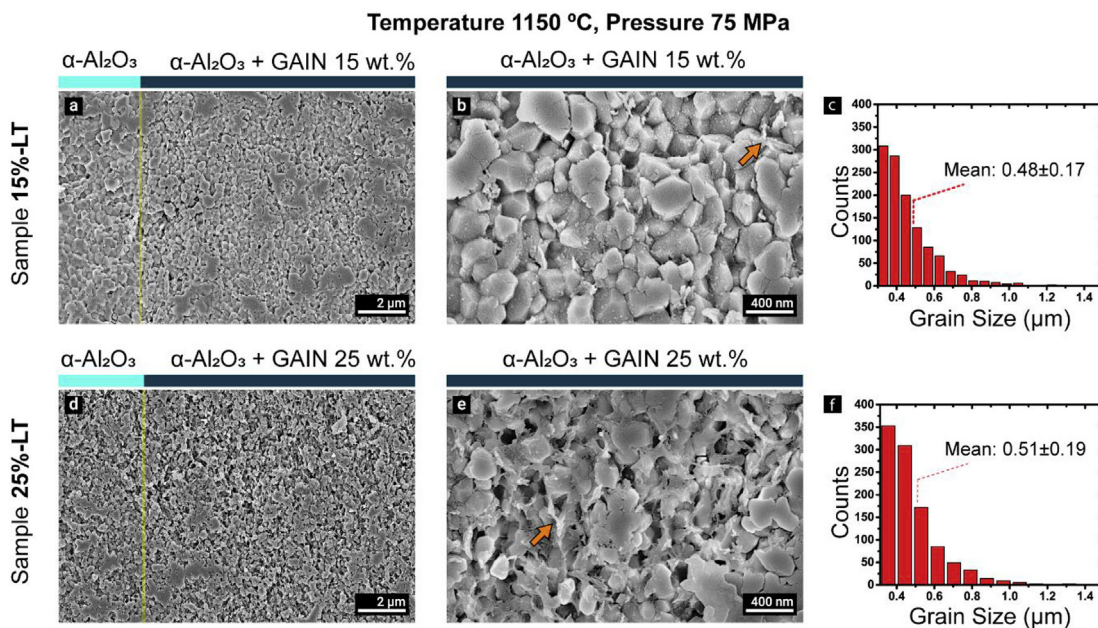


**Fig. 3.** SEM micrograph of SPS samples sintered at 1150 °C under 70 MPa; (a,d) interface between the hybrid layer and monolithic  $\alpha\text{-Al}_2\text{O}_3$ , (b,e) interlayer in the sample with 15 and 25 wt % GAIN respectively-arrows pointing at GAIN fibers in the microstructure, (c,f) interlayer grain size distribution in samples with 15 and 25 wt % GAIN, respectively. (A colour version of this figure can be viewed online.)



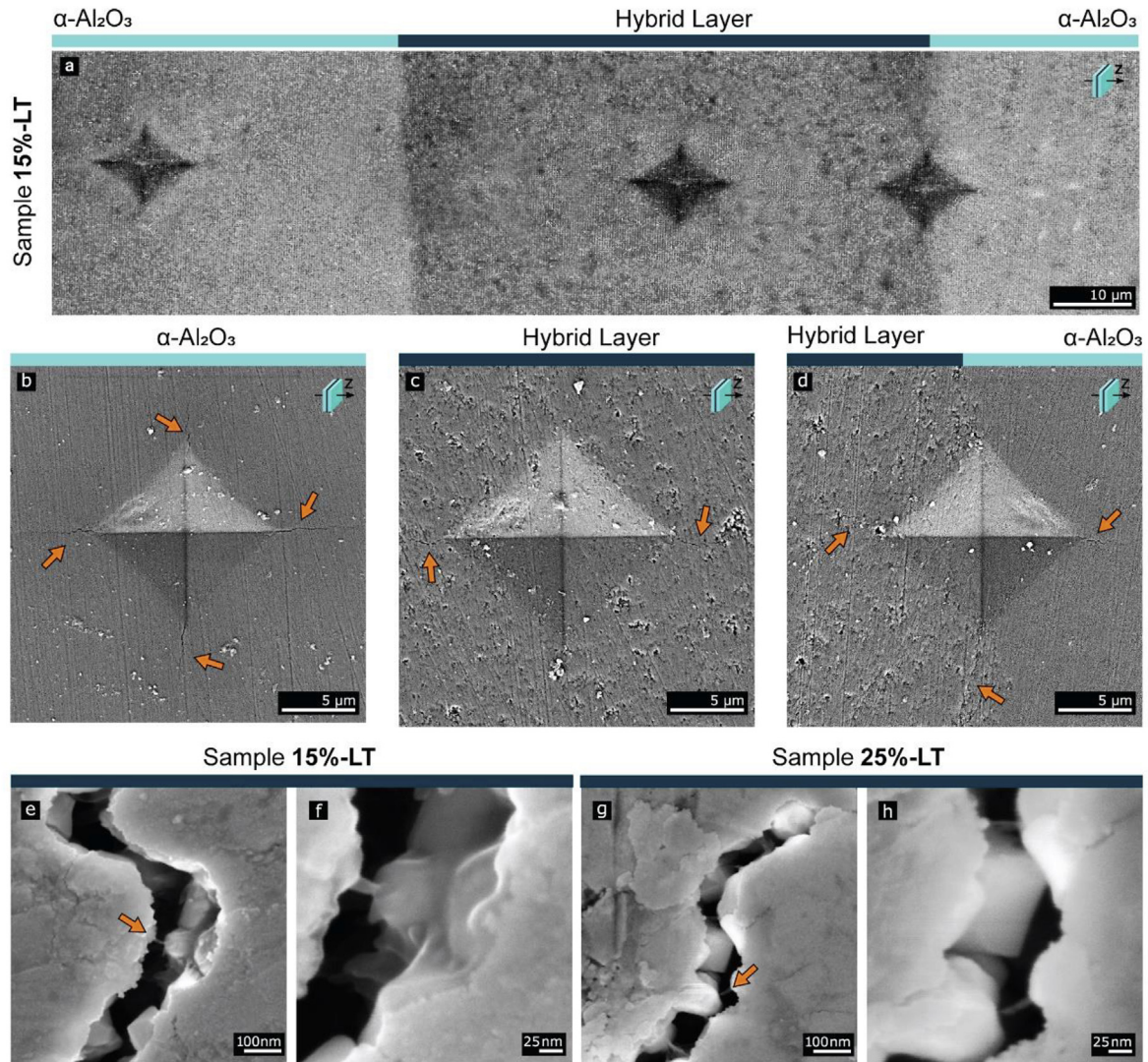


**Fig. 4.** (a) OM image of the Vicker's microhardness imprints, and SEM images of crack propagation from the sites of the indentations in the (b) monolithic  $\text{Al}_2\text{O}_3$ , (c) hybrid interlayer, (d) interface between the monolithic  $\text{Al}_2\text{O}_3$  and the hybrid layer – arrows pointing at the propagated cracks, Fiber bridging in the interlayer of LT samples with (e,f) 15 and (g,h) 25 wt % GAIN, respectively. (A colour version of this figure can be viewed online.)

**Table 2**

Mechanical properties of the hybrid interlayer, monolithic  $\alpha\text{-Al}_2\text{O}_3$ , and the interface between the two layers.

Sample Name	Relative Density	Monolithic Alumina			Hybrid layer			Interface
		H [GPa] <sup>a</sup>	E [GPa] <sup>b</sup>	W <sub>e</sub> [%] <sup>c</sup>	H [GPa] <sup>a</sup>	E [GPa] <sup>b</sup>	W <sub>e</sub> [%] <sup>c</sup>	
25%-LT	>99%	24.5 ± 0.7	475.1 ± 28.2	0.38 ± 0.03	11.3 ± 0.8	343.3 ± 29.7	0.29 ± 0.04	17.7 ± 0.5
25%-HT	99%	23.3 ± 0.5	451.2 ± 4.3	0.32 ± 0.06	17.7 ± 0.9	306.1 ± 63.1	0.26 ± 0.07	22.2 ± 0.9
15%-LT	>99%	24.5 ± 0.6	481.1 ± 14.1	0.36 ± 0.02	22.2 ± 0.5	356.1 ± 16.9	0.24 ± 0.05	24.5 ± 0.8
15%-HT	99%	22.2 ± 0.5	426.5 ± 34.8	0.37 ± 0.02	21.2 ± 0.8	326.7 ± 33.6	0.23 ± 0.05	22.2 ± 0.7

<sup>a</sup> Hardness (HV0.5 Microhardness).

<sup>b</sup> Modulus of Elasticity.

<sup>c</sup> Elastic Recovery.

SPS together with the opposite behavior of the coefficient of thermal expansion (CTE) of graphene and alumina, which result in CTE mismatch during the cooling process, promotes crack deflection and pinning. Fig. 4c demonstrates the cracks in the hybrid layer (15%-LT), which propagate in perpendicular direction to the interlayer plane (parallel to SPS pressure axis) indicating a weak c-axis intergranular interface. No developed crack system is observed parallel to the plane pointing at an increased toughness in the area

added by the fibers. Fig. 4d demonstrates the cracks evolved parallel to the hybrid layer plane at the interface. In Fig. 4e-h, the fibers pull-out combined with crack' bridging can be considered as one of the toughening mechanisms.

The load-unload curves, fitted with the standard Oliver-Pharr procedure [36], are presented in Fig. 5a and b for the alumina and hybrid layers. Modulus of elasticity  $E$  was calculated using Equation (2), and reduced modulus  $E'$  (effective contact stiffness)

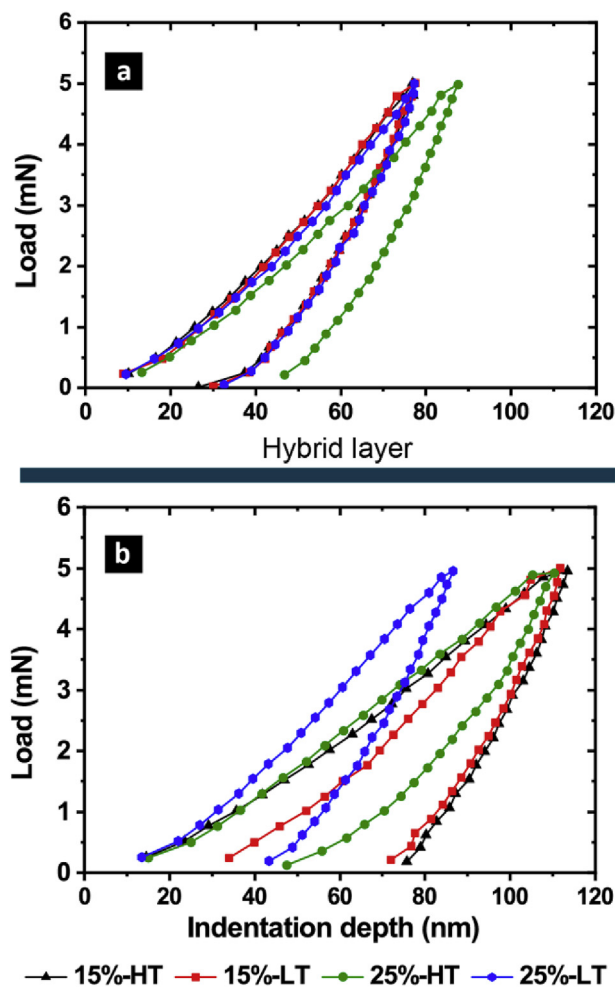


Fig. 5. Loading-Unloading nanoindentation curves for; (a)  $\text{Al}_2\text{O}_3$  layers and (b) hybrid interlayers. (A colour version of this figure can be viewed online.)

was obtained from the nanoindentation test data. Fig. 5a displays an identical behavior of all samples except the sample 25%-HT with a slightly wider area under the curve and, correspondingly, a lower hardness of 21 GPa. The samples with 25 wt% GAIN reveal a higher elastic recovery in the interlayer area as compared to the samples with 15 wt% GAIN, which can be attributed to the increased level of porosity in the former case. While the modulus of elasticity of the monolithic alumina matches the reference data, the sample sintered at 1150 °C with 15 wt% GAIN shows an enhancement in both hardness and modulus.

$$E' = \left\{ (1 - \nu_s^2) / E_s + (1 - \nu_i^2) / E_i \right\}^{-1} \quad (2)$$

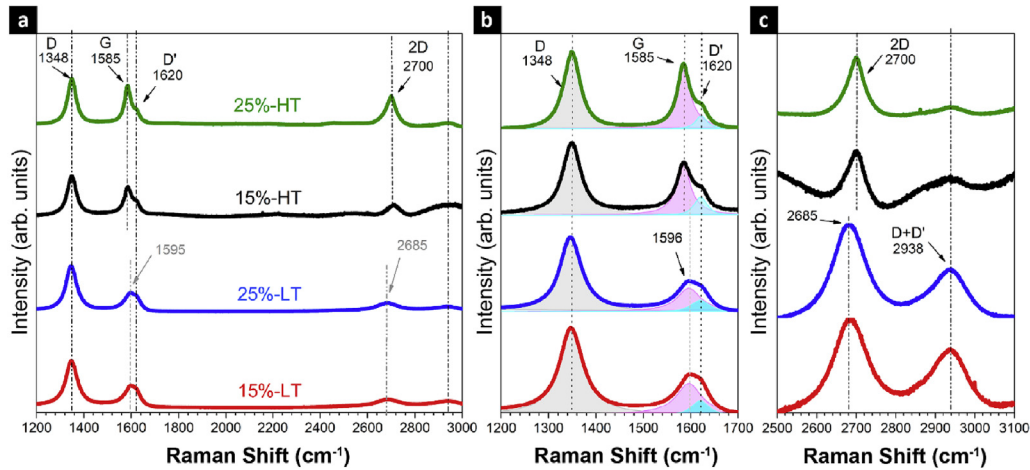
### 3.3. Raman spectroscopy

Fig. 6 displays Raman spectra of the interlayers of the samples recorded using a 532 nm laser. Raman spectra of the GAIN fibers is presented in Fig. S1b (see Supplementary information, S1). All samples have demonstrated the main features of both graphene and bulk graphite, represented by G and 2D peaks. The G peak is driven by the high frequency  $E_{2g}$  phonons at  $\Gamma$  point of the Brillouin zone and is due to the stretching of the C–C bond in  $\text{sp}^2$  atoms causing in-plane vibrations [37]. The disorder-induced D peak at  $1348 \text{ cm}^{-1}$  corresponds to breathing modes of  $\text{sp}^2$  atoms in the

rings and can be used to monitor disorder in  $\text{sp}^2$ -hybridized carbon systems [37,38]. The D' shoulder at the G peak at  $\sim 1620 \text{ cm}^{-1}$  is denoted to be in connection with the double resonance condition, when energy is conserved in multiple transitions (electron/hole pair, electron-phonon scattering, and defect scattering) producing phonons with small wave vector, which is characteristic of defected graphite [39].

In Fig. 6b, Pseudo-Voigt fitting has been carried out to show only the peak position of each component, whereas areas under the spectra have not been considered for any discussion. Granted that the  $I(D)/I(G)$  ratio is slightly higher for LT samples, it presumably is a result of a higher population of nanoscale defects present under the laser spot [40] attributed to the different grain size distribution in the interlayer. The double resonant Raman scattering theory suggests that the  $I(D)/I(D')$  is associated with the following defect types: (i)  $\text{sp}^3$  defects ( $\sim 13$ ), (ii) hopping defects ( $\sim 10.5$ ), (iii) vacancy-like defects ( $\sim 3.5$ ), and (iv) on-site defects ( $\sim 1.3$ ) [41,42]. The  $I(D)/I(D')$  ratio for all samples is between  $\sim 2.7$  and  $\sim 3.2$  with no observable impact of the sintering conditions which suggests a combined vacancy-like and on-site defected structure. The position of the G peak is shifted in the LT samples, which can be attributed to unintentional electron, and hole doping levels of the GAIN fibers, both resulting in a red-shift of the G mode [43,44]. This assumption is consistent with the p-type conduction of the hybrid interlayer at room temperature and a sign inversion of the Hall mobility in the GAIN fillers below room temperature discussed in section 3.4.1. On the other hand, the  $I(G)$  is proportional to the amount of  $\text{sp}^2$  rings and its decrease can correspond to  $\text{sp}^3$  formation [45]. Moreover, an increase in  $I(D)/I(G)$  and  $I(D')/I(G)$  ratios occurs by  $\text{sp}^3$  formation [42]. The proposed concept is valid when comparing samples sintered at 1450 °C to those sintered at 1150 °C. For example, the  $I(D)/I(G)$  ratios for the samples 25%-HT and 25%-LT are  $\sim 1.18$  and  $\sim 2.62$  respectively. An increase is also observed for  $I(D')/I(G)$  ratios for the same samples having the values of  $\sim 0.04$  and  $0.83$ , respectively. Correlating the increased ratios in LT samples with decrease observed in  $E_{2g}$  band, a transition from nanocrystalline graphite to low  $\text{sp}^3$  hybridization can be justified.

The second order of the D peak in bulk graphite consists of two components; whereas in all four samples, a single 2D peak is detected, which may correspond to either monolayer or few layer graphene. The 2D band in graphene at  $\sim 2670 \text{ cm}^{-1}$  is caused by double resonance scattering of TO phonons at the k-point of the zone edge [46]. For multi-layered graphene, the 2D peak is about four times stronger than the G peak at  $\sim 1585$  (the wider the peak gets at 2D region, the more layers of graphene are expected) [39]. For the tested structures, the  $I(2D)/I(G)$  ratio (visible in Fig. 6a) is roughly  $\frac{1}{2}$  with smallest FWHM of  $\sim 49$  in HT samples, suggesting a more ordered graphene structure with the higher temperature of sintering. The normalized 2D peaks in samples sintered at 1450 °C show a  $20 \text{ cm}^{-1}$  red-shift marked with vertical dash lines in Fig. 6c. The red-shift agrees with results for turbostratic graphite [37], however, in the GAIN samples it is more likely to be a result of strain caused by interaction with substrate. The position of the 2D peak and the corresponding shift agrees with the results for graphene on sapphire in Ref. [47]. Functionalization of graphene with hydrogen and  $\text{sp}^3$  hybridization introduce a peak at  $\sim 2930 \text{ cm}^{-1}$ . For the HT samples a lower D + D' intensity, a  $20 \text{ cm}^{-1}$  red-shift of the 2D band, and the existing fluorescence slope (the slope is normalized in the graphs) may serve as possible indicators of purification of C–H bonding (dehydrogenation) which are  $\text{sp}^3$  hybridized in LT samples. In other words, the hydrogen functionalized GAIN fibers are better purified in HT samples showing a higher  $I(2D)/I(G)$  ratio, narrower FWHM of the 2D, and flatter D + D' peak. In the LT samples the decreased  $I(G)$  and increased  $I(D')/I(G)$  and  $I(D)/I(G)$  ratios indicate possible  $\text{sp}^3$  hybridization while the red-shifted G peak suggests



**Fig. 6.** Raman spectra of the interlayer in the samples with 15 and 25 wt% loading of GAIN. (a) Average Raman spectra of the interlayers in LT (1150 °C) with 15 (red-line) and 25 (blue-line) wt.% loading of GAIN and at HT (1450 °C) with 15 (black-line) and 25 (green-line) wt.% GAIN. Comparison of the Raman spectra of interlayer of the samples: (b) Detail of the Raman spectra in the wavenumber ranging from 1200 to 1700  $\text{cm}^{-1}$  comparing the 2D and D + D' peaks. (c) Raman spectra in the Raman shift wavenumber range from 2500 to 3100  $\text{cm}^{-1}$ . (A colour version of this figure can be viewed online.)

higher doping level possibly corresponding to higher concentration of hydrogen bonding.

### 3.4. Electrical transport properties

#### 3.4.1. Hall measurement

A GAIN fibrous specimen was manually pressed and mounted

onto the probe of PPMS. Resistance and Hall measurement data are shown in Fig. 7a and b. Due to a low linear density perpendicular to the rods, resistivity values do not represent the inherent properties of the GAIN fibers. Therefore, in Fig. 7a, the temperature dependence of the absolute values (resistance) is demonstrated. A well pronounced semiconducting behavior is apparent from Fig. 7a, reflecting the intrinsic contribution of a bulk-graphite-like

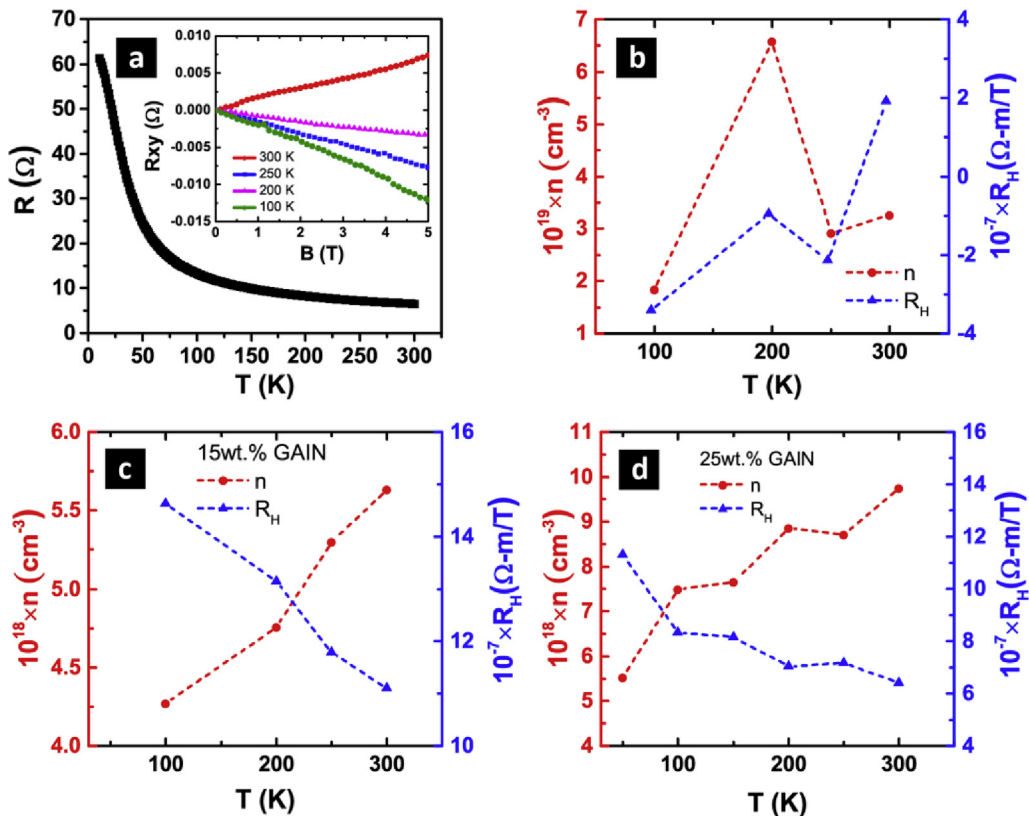


**Fig. 7.** Electrical transport and Hall measurement: (a) temperature dependency of DC resistance of GAIN fibers; Inset: Hall resistance as a function of magnetic field, Temperature dependency of Hall coefficient and carriers' density in (b) GAIN fibers, (c) alumina composite with 15 wt% GAIN, (d) alumina composite with 25 wt% GAIN. (A colour version of this figure can be viewed online.)



conduction [48] with a narrow band gap of 5.6 meV, which was calculated from the slope of the line of Arrhenius plot. In practice, polycrystalline graphene samples contain various types of disorder, such as point defects, contaminations and impurities that degrade the mobility in comparison to single-crystalline graphene. In section 3.3, the presence of such impurities was discussed. In fact, GBs in polycrystalline graphene largely impede carriers' transport, while they are often n-doped as compared to the nearby p-type graphene grains (due to contribution of surface adsorbates and contaminants). As a result, between the GB and graphene grains at small scales p-n junctions are formed that modulate the bandgap [49–51]. The power-law dependent semiconducting behavior and the absence of a temperature crossover indicates no transition in transport mechanism (e.g. semiconducting to metallic) and, therefore, no direct contribution of the Dirac point can be stated. This behavior is often correlated to the presence of structural impurities such as H bonding and substrate effect on the transport of CVD graphene. In the Hall resistance vs field plot (Fig. 7a, inset), no plateau is observed up to 5 T which indicates absence of Quantum Hall Effect (QHE) attributed to the three dimensional characteristics of the system under study, as well as the multilayer polycrystalline graphene. In fact, in three dimensions, the QHE is forbidden since the absence of quantum confinement spreads Landau levels into overlapping bands, which results in diminished quantization [52].

In Fig. 7b, the Hall coefficient visibly undergoes a sign inversion in the temperature interval of 250–280K and persists up to room temperature. The n-doping in this case is consistent with transport in hydrogenated graphene also reported for SiO<sub>2</sub> substrate [53]. The n-type behavior is a result of a decrease in the work function (WF) of hydrogenated graphene as compared to pristine graphene relative to the substrate's WF [53]. In contrast, p-doping is often correlated to physisorbed water on the surface of the graphene [53]. It was shown in Ref. [54] that wettability of CVD graphene is strongly dependent on the substrate while a decrease in water contact angle to  $\leq 60^\circ$ , shifts the fermi level from n-to p-type. This phenomenon can describe the p-type transport at room temperature in GAIN fibers where liquid physisorbed water is present. On the other hand, the temperature interval of 250–280K where the Hall coefficient sign inversion occurs is around the freezing point of water. Granted that the physisorbed ice on graphene does not contribute to neither of short- or long-range scatterings and to charge donation [55], at temperatures lower than the freezing point, the intrinsic electron contribution to the transport is consistent with the theoretical and experimental models for hydrogenated/few layers of graphene (Fig. 7a and b) [53,56]. In addition, Song et al. demonstrated that the water between graphene layers at a distance of 4.5 Å n-dopes the graphene, while p-doping occurs when the distance is reduced to 4 Å [57].

The sign inversion observed for GAIN fillers is superseded by a constant p-type conduction across the temperature range in composites with 15 and 25 wt% GAIN in Al<sub>2</sub>O<sub>3</sub> matrix, visible from the positive values of  $R_H$  in Fig. 7c, and d respectively. One plausible explanation could be the strong interaction of the  $\alpha$ -alumina matrix with graphene, which induces p-doping in the presence of electron accepting impurities such as Fe<sup>+</sup> and point defects such as aluminum interstitials and oxygen vacancies. The phenomenon was reported for Few-Layer Graphene/Al<sub>2</sub>O<sub>3</sub> [56] in which the mechanism of the strong interaction of the graphene with the matrix was justified by the opposite linear thermal expansion behavior of alumina and graphene during the cooling process of sintering causing residual stress acting upon them [56].

It is shown that optical phonons at the graphene/substrate interface of monolayer and bilayer graphene modulate the polarization of the transport. It is also shown that intervalley scattering (consistent with observed D peak in section 3.3, which require the

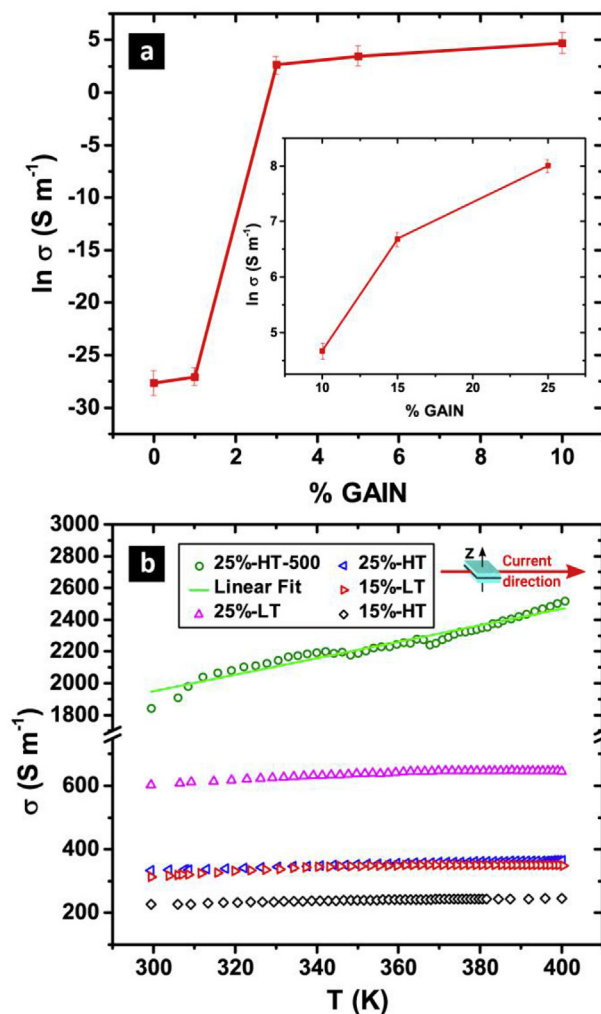


**Fig. 8.** (a) Electrical conductivity percolation threshold of composites of GAIN/Al<sub>2</sub>O<sub>3</sub>; inset: conductive fillers fraction effect on electrical conductivity. (b) DC in-plane electrical conductivity as a function of temperature. (A colour version of this figure can be viewed online.)

same scattering mechanism) and backscattering are the dominant transport mechanisms in polycrystalline graphene where GBs are present [51]. Having those in mind, increasing temperature enables surface phonon modes, which reduce mobility to a great extent. However, additional graphene layers in few layer polycrystalline graphene effectively screen the electric field of the substrate phonons. As a result, the mobility increases with temperature while the dominant mobility mechanism is Coulomb scattering [58–60]. Both optical and acoustic phonons can give rise to in-between states transitions in conduction band valleys. However, the energy scales of longitudinal acoustic phonons are too high to cause an effective scattering channel comparing to those posed by Coulomb and optical phonons. Therefore, their contribution can be neglected for multilayer graphene [61].

### 3.4.2. DC properties

Fig. 8 presents the dc electrical conductivity data of the layered structures obtained using two-probe in-plane measurement from room temperature to 400 K. As it is shown in Fig. 8a, estimated experimental percolation threshold for electrical conductivity is around 3 wt% of the fillers. This amount accounts for about 0.39 wt % of the total calculated carbon content detailed in Ref. [12]. In this

work, volume fraction dependence of the conductive fillers and their size effect on the percolation threshold is in agreement with the experimental and theoretical models [62]. Fig. 8a, inset, demonstrates that increasing the amount of the fillers drastically increases the electrical conductivity which at 25 wt% fillers' fraction (3.25 wt% carbon) the value reaches  $3000 \text{ S m}^{-1}$  in a bulk composite. This value is two folds of magnitude higher than the reported data for 3.7 vol% MWCNT/ $\text{Al}_2\text{O}_3$  [63] but in-between the values reported for graphene nano pellets [64] and reduced graphene oxide [56]. It is also shown that electrical properties vary in the case of integrating thin graphene/alumina layers into monolithic alumina as compared to bulk composites, suggesting thickness dependency (Fig. 8b). Decrease in the layer thickness results in reduced conductivity. This effect can be explained by random orientation of the conductive fibers with slight preferred orientation perpendicular to the sintering pressure axis. Transport in the direction perpendicular to the pressure axis ( $\sigma^\perp$ ) is considered to be through hopping mechanism. Whereas, in parallel direction ( $\sigma^\parallel$ ), a more complex mechanism and significant contribution of grain boundaries (i.e. graphene grains discussed in section 3.4.1) is a more plausible interpretation [65]. Expectedly, multi layered graphene has a much higher in plane conductivity compared to c-axis transport perpendicular to the honeycomb basal planes. The  $\sigma^\perp$ : $\sigma^\parallel$  is also reported to be dependent on the fillers' content and increase by increasing their fraction [65,66]. This effect is more noticeable for the sample 25%-HT-500 with 500  $\mu\text{m}$  interlayer thickness and 25 wt% GAIN. This anisotropy should not be confused with the macroscopic  $\sigma^\parallel$ : $\sigma^\perp$  of the layered structures, which is a measure of the in-plane conductivity of the samples vs. perpendicular conductivity of  $\sim 10^{-12} \text{ S m}^{-1}$  corresponding to monolithic alumina. In the meantime, a more prominent increase in the conductivity of the same sample over temperature signals a better semiconducting behavior as compared to other samples with 100  $\mu\text{m}$  interlayer thickness. That is to say, a more graphite like behavior of the thicker interlayer complies with increased 3rd dimensionality of the transport system due to accumulation of the stacked graphene coated fillers in the 500  $\mu\text{m}$  hybrid interlayer. On the other hand, the sintering conditions influence the transport in the hybrid layer due to different grain growth rate. More specifically, as discussed in section 3.1, sintering at low temperature prohibits grain growth to a great extent and subsequently carrier transport is less disturbed based on two reasons; (I) samples sintered at higher temperature undergo significant grain growth which corresponds to large amounts of GBs defects. Thicker and defected GBs influence the carrier transport, which results in an increased resistivity. (II) Based on the theoretical evidence [31], a transition from  $\gamma$  to  $\alpha$  phase in the  $\text{Al}_2\text{O}_3$  fibers is presumed at sintering temperatures higher than 1200 °C. This transition results in linearly aligned granules of  $\alpha$ - $\text{Al}_2\text{O}_3$  particles rather than fibrous structure, which greatly acts as a barrier for the carrier transport. The latter case, yet to be confirmed by the means of transfer electron microscopy in our structures. The modification of transport in LT samples is in spite of Raman spectroscopy results where for LT samples, increase in  $I(\text{D})/I(\text{G})$  and  $I(\text{D}')/I(\text{G})$  together with observed D + D' peak was correlated to the  $\text{sp}^3$  hybridization and C–H bonding.

#### 4. Conclusions

In this work, a novel approach detailing the fabrication of the anisotropic functional multi-layered structures was implemented by ex-situ stacking alternative layers of  $\alpha$ -alumina and hybrid interlayers, which consist of graphene-augmented  $\gamma$ -alumina nanofibers and  $\alpha$ -alumina nanoparticles. A straight-forward bottom-up method based on catalyst-free hot-wall CVD process was employed to obtain the graphene-augmented nanofibers applied as

conductive fillers in the hybrid interlayer. The strategy to develop multilayered structures, introduces in-plane electrical conductivity in an otherwise insulating alumina preserving the mechanical properties of the bulk. Fully dense fine-grained materials were produced by SPS, employing both low (1150 °C) and high (1450 °C) temperature regimes. An excellent combination of high hardness (21–22 GPa) and modulus of elasticity (326–356 GPa) for a sample with 15 wt% of graphene augmented fillers in the hybrid layers obtained by means of the low and high temperature methods. However, in both sintering approaches, the presence of conductive fillers refines the microstructure by inhibition of grain growth not only in the hybrid interlayer but also with a slight influence on the monolithic alumina layers. Electrons were the dominant carriers in the graphene augmented nano-fillers, however in the composites, strong p-doping of alumina matrix resulted in p-type conduction. Transport in thinner interlayers shows a tendency towards semi-metallic behavior from RT to 400K. It was shown that increase in the fillers fraction results in increased conductivity from the percolation threshold at 0.39 wt% of the calculated carbon content in a full composite to in-plane  $\sim 600$  and  $1800 \text{ S m}^{-1}$  in the 100 and 500  $\mu\text{m}$  thick interlayers of the multilayered structures, respectively, employing a calculated 3.25 wt% of carbon content. In the same multilayered materials, a significant macroscopic anisotropy is achieved, where  $\sigma^\perp$  (perpendicular to the hybrid interlayer and parallel to SPS pressure axis) equals to that of highly resistive monolithic alumina. A simple adjustment of the processing conditions, thickness and amount of graphene fillers, allows tuning the electrical response, which can help designing functional materials with potential application in areas such as EMI-shielding for electronics and aerospace.

#### CRediT authorship contribution statement

**Ali Saffar Shamshirgar:** Investigation, Methodology, Writing - original draft, Validation. **Rocio Estefania Rojas Hernández:** Investigation. **Girish C. Tewari:** Investigation. **Roman Ivanov:** Investigation, Validation. **Valdek Mikli:** Investigation. **Maarit Karppinen:** Data curation. **Irina Hussainova:** Conceptualization, Writing - review & editing, Supervision.

#### Declaration of competing interest

The authors declare that they have no known competing financial interests or personal relationships that could have appeared to influence the work reported in this paper.

#### Acknowledgements

This work was supported by the Estonian Research Council under PRG643 (I. Hussainova), and the Estonian Ministry of Higher Education and Research under Projects IUT19-29, TK-141 and IUT19-28. Rocio E. Rojas-Hernandez acknowledges the financial support of the Mobilitas Plus program in the framework of the MOBJD254 project. The authors would like to acknowledge the help of Dr. Olga Volobujeva from Department of Materials and Environmental Technologies, TalTech, for SEM imaging and Mart Viljus from Department of Mechanical and Industrial Engineering, TalTech, for grain size analysis.

#### Appendix A. Supplementary data

Supplementary data to this article can be found online at <https://doi.org/10.1016/j.carbon.2020.06.038>.

## References

- [1] U.G.K. Wegst, H. Bai, E. Saiz, A.P. Tomsia, R.O. Ritchie, Bioinspired structural materials, *Nat. Mater.* 14 (2015) 23–36, <https://doi.org/10.1038/nmat4089>.
- [2] Z. Liu, M.A. Meyers, Z. Zhang, R.O. Ritchie, Functional gradients and heterogeneities in biological materials: design principles, functions, and bioinspired applications, *Prog. Mater. Sci.* 88 (2017) 467–498, <https://doi.org/10.1016/j.pmatsci.2017.04.013>.
- [3] H.D. Espinosa, J.E. Rim, F. Barthelat, M.J. Buehler, Merger of structure and material in nacre and bone – perspectives on de novo biomimetic materials, *Prog. Mater. Sci.* 54 (2009) 1059–1100, <https://doi.org/10.1016/j.pmatsci.2009.05.001>.
- [4] M. Zhou, H. Bi, T. Lin, X. Lü, F. Huang, J. Lin, Directional architecture of graphene/ceramic composites with improved thermal conduction for thermal applications, *J. Mater. Chem. A* 2 (2014) 2187–2193, <https://doi.org/10.1039/c3ta14325b>.
- [5] C. Molin, P. Neumeister, H. Neubert, S.E. Gebhardt, Multilayer Ceramics for Electrocaloric Cooling Applications, *Energy Technol.* 2018, pp. 1–11, <https://doi.org/10.1002/ente.201800127>.
- [6] H. Luo, P. Xiao, W. Hong, Dielectric behavior of laminate-structure C<sub>f</sub>/Si<sub>3</sub>N<sub>4</sub> composites in X-band, *Appl. Phys. Lett.* 105 (2014) 172903, <https://doi.org/10.1063/1.4900932>.
- [7] H. Porwal, P. Tatarko, S. Grasso, J. Khaliq, I. Dlouhý, M.J. Reece, Graphene reinforced alumina nano-composites, *Carbon N. Y.* 64 (2013) 359–369, <https://doi.org/10.1016/j.carbon.2013.07.086>.
- [8] R. Ivanov, I. Hussainova, M. Aghayan, M. Drozdova, D. Pérez-Coll, M.A. Rodríguez, F. Rubio-Marcos, Graphene-encapsulated aluminium oxide nanofibers as a novel type of nanofillers for electroconductive ceramics, *J. Eur. Ceram. Soc.* 35 (2015) 4017–4021, <https://doi.org/10.1016/j.jeurceramsoc.2015.06.011>.
- [9] A.K. Geim, K.S. Novoselov, The rise of graphene, *Nat. Mater.* 6 (2007) 183–191, <https://doi.org/10.1038/nmat1849>.
- [10] A. Nieto, L. Huang, Y.H. Han, J.M. Schoenung, Sintering behavior of spark plasma sintered alumina with graphene nanoplatelet reinforcement, *Ceram. Int.* 41 (2015) 5926–5936, <https://doi.org/10.1016/j.ceramint.2015.01.027>.
- [11] C. Ramírez, S.M. Vega-Díaz, A. Morelos-Gómez, F.M. Figueiredo, M. Terrones, M.I. Osendi, M. Belmonte, P. Miranzo, Synthesis of conducting graphene/Si<sub>3</sub>N<sub>4</sub> composites by spark plasma sintering, *Carbon N. Y.* 57 (2013) 425–432, <https://doi.org/10.1016/j.carbon.2013.02.015>.
- [12] M. Drozdova, I. Hussainova, D. Pérez-Coll, M. Aghayan, R. Ivanov, M.A.A. Rodríguez, A novel approach to electroconductive ceramics filled by graphene covered nanofibers, *Mater. Des.* 90 (2016) 291–298, <https://doi.org/10.1016/j.matdes.2015.10.148>.
- [13] A. Centeno, V.G. Rocha, B. Alonso, A. Fernández, C.F. Gutierrez-Gonzalez, R. Torrecillas, A. Zurutuza, Graphene for tough and electroconductive alumina ceramics, *J. Eur. Ceram. Soc.* 33 (2013) 3201–3210, <https://doi.org/10.1016/j.jeurceramsoc.2013.07.007>.
- [14] I. Hussainova, M. Drozdova, D. Pérez-Coll, F. Rubio-Marcos, I. Jasiuk, J.A.N.T. Soares, M.A. Rodríguez, Electroconductive composite of zirconia and hybrid graphene/alumina nanofibers, *J. Eur. Ceram. Soc.* 37 (2017) 3713–3719, <https://doi.org/10.1016/j.jeurceramsoc.2016.12.033>.
- [15] Y. Kim, J. Lee, M.S. Yeom, J.W. Shin, H. Kim, Y. Cui, J.W. Kysar, J. Hone, Y. Jung, S. Jeon, S.M. Han, Strengthening effect of single-atomic-layer graphene in metal–graphene nanolayered composites, *Nat. Commun.* 4 (2013) 2114, <https://doi.org/10.1038/ncomms3114>.
- [16] J. Ru, Y. Fan, W. Zhou, Z. Zhou, T. Wang, R. Liu, J. Yang, X. Lu, J. Wang, C. Ji, L. Wang, W. Jiang, Electrically conductive and mechanically strong graphene/mullite ceramic composites for high-performance electromagnetic interference shielding, *ACS Appl. Mater. Interfaces* 10 (2018) 39245–39256, <https://doi.org/10.1021/acsami.8b12933>.
- [17] B. Luo, X. Wang, E. Tian, H. Gong, Q. Zhao, Z. Shen, Y. Xu, X. Xiao, L. Li, Dielectric enhancement in graphene/barium titanate nanocomposites, *ACS Appl. Mater. Interfaces* 8 (2016) 3340–3348, <https://doi.org/10.1021/acsami.5b11231>.
- [18] M. Belmonte, A. Nistal, R. Cruz-Silva, A. Morelos-Gómez, M. Terrones, P. Miranzo, M.I. Osendi, Directional electrical transport in tough multifunctional layered ceramic/graphene composites, *Adv. Electron. Mater.* 1 (2015) 1500132, <https://doi.org/10.1002/aeml.201500132>.
- [19] P. Miranzo, E. García, C. Ramírez, J. González-Julián, M. Belmonte, M. Isabel Osendi, Anisotropic thermal conductivity of silicon nitride ceramics containing carbon nanostructures, *J. Eur. Ceram. Soc.* 32 (2012) 1847–1854, <https://doi.org/10.1016/j.jeurceramsoc.2012.01.026>.
- [20] P. Rutkowski, P. Klimczyk, L. Jaworska, L. Stobierski, A. Dubiel, Thermal properties of pressure sintered alumina–graphene composites, *J. Therm. Anal. Calorim.* 122 (2015) 105–114, <https://doi.org/10.1007/s10973-015-4694-x>.
- [21] S.N. Stamatini, I. Hussainova, R. Ivanov, P.E. Colavita, Quantifying graphitic edge exposure in graphene-based materials and its role in oxygen reduction reactions, *ACS Catal.* 6 (2016) 5215–5221, <https://doi.org/10.1021/acscatal.6b00945>.
- [22] I. Hussainova, R. Ivanov, S.S. Kale, I. Jasiuk, Tunneling–Percolation Behavior of Graphene-Encapsulated Whiskers as Electroconductive Fillers for Ceramics, Springer International Publishing, Cham, 2019, <https://doi.org/10.1007/978-3-030-00868-0>.
- [23] M. Aghayan, I. Hussainova, M. Gasik, M. Kutuzov, M. Friman, Coupled thermal analysis of novel alumina nanofibers with ultrahigh aspect ratio, *Thermochim. Acta* 574 (2013) 140–144, <https://doi.org/10.1016/j.tca.2013.10.010>.
- [24] Z. Shen, M. Johansson, Z. Zhao, M. Nygren, Spark plasma sintering of alumina, *J. Am. Ceram. Soc.* 85 (2002) 1921–1927, <https://doi.org/10.1111/j.1151-2916.2002.tb00381.x>.
- [25] A.S. Shamshirgar, R. Ivanov, I. Hussainova, Spark plasma sintering of layered  $\gamma$ -Al<sub>2</sub>O<sub>3</sub>/graphene reinforced nanocomposites, *Proc. Est. Acad. Sci.* 68 (2019) 140, <https://doi.org/10.3176/proc.2019.2.04>.
- [26] M. Prakasam, D. Michau, O. Viraphong, M. Prakasam, D. Michau, O. Viraphong, A. Largeau, Optimal Sintering Parameters for Al<sub>2</sub>O<sub>3</sub>/Optoceramics with High Transparency by Spark Plasma Sintering Optimal Sintering Parameters for Al<sub>2</sub>O<sub>3</sub>/Optoceramics with High Transparency by Spark Plasma Sintering, 2016, p. 6753, <https://doi.org/10.1080/17436753.2016.1149909>.
- [27] I. Hussainova, E. Hamed, I. Jasiuk, Nanoindentation testing and modeling of chromium-carbide-based composites, *Mech. Compos. Mater.* 46 (2011) 667–678, <https://doi.org/10.1007/s11029-011-9180-3>.
- [28] H.P.R. Frederikse, W.R. Hosler, High temperature electrical conductivity of aluminum oxide, *Mass Transp. Phenom. Ceram.*, Springer US, Boston, MA, 1975, pp. 233–252, [https://doi.org/10.1007/978-1-4684-3150-6\\_16](https://doi.org/10.1007/978-1-4684-3150-6_16).
- [29] J.F. Shackelford, Y.-H. Han, S. Kim, S.-H. Kwon, CRC Materials Science and Engineering Handbook, CRC Press, 2016, <https://doi.org/10.1201/b18971>.
- [30] M. Tokita, Spark plasma sintering (SPS) method, systems, and applications, in: *Handb. Adv. Ceram.*, Elsevier, 2013, pp. 1149–1177, <https://doi.org/10.1016/B978-0-12-385469-8.00060-5>.
- [31] E. Yalapan, A. Trapani, S. Akkurt, Sintering and microstructural investigation of gamma-alpha alumina powders, *Eng. Sci. Technol. an Int. J.* 17 (2014) 2–7, <https://doi.org/10.1016/j.jestch.2014.02.001>.
- [32] S. Lamouri, M. Hamidouche, N. Bouadouja, H. Belhouichet, V. Garnier, G. Fantozzi, J.F. Trelkat, Control of the  $\gamma$ -alumina to  $\alpha$ -alumina phase transformation for an optimized alumina densification, *Bol. La Soc. Esp. Ceram. y Vidr.* 56 (2017) 47–54, <https://doi.org/10.1016/j.bsecv.2016.10.001>.
- [33] M. Estili, Y. Sakka, Recent advances in understanding the reinforcing ability and mechanism of carbon nanotubes in ceramic matrix composites, *Sci. Technol. Adv. Mater.* 15 (2014), <https://doi.org/10.1088/1468-6996/15/6/064902>, 064902.
- [34] J. Silvestre, J. de Brito, An overview on the improvement of mechanical properties of ceramics nanocomposites, *J. Nanomater.* 2015 (2015) 1–13, <https://doi.org/10.1155/2015/106494>.
- [35] S. Ganizadeh, S. Grasso, P. Ramanujam, B. Vaidhyanathan, J. Binner, P. Brown, J. Goldwasser, Improved transparency and hardness in  $\alpha$ -alumina ceramics fabricated by high-pressure SPS of nanomaterials, *Ceram. Int.* 43 (2017) 275–281, <https://doi.org/10.1016/j.ceramint.2016.09.150>.
- [36] W.C. Oliver, G.M. Pharr, An improved technique for determining hardness and elastic modulus using load and displacement sensing indentation experiments, *J. Mater. Res.* 7 (1992) 1564–1583, <https://doi.org/10.1557/JMR.1992.1564>.
- [37] A.C. Ferrari, D.M. Basko, Raman spectroscopy as a versatile tool for studying the properties of graphene, *Nat. Nanotechnol.* 8 (2013) 235–246, <https://doi.org/10.1038/nnano.2013.46>.
- [38] A.A.K. King, B.R. Davies, N. Noorbehesht, P. Newman, T.L. Church, A.T. Harris, J.M. Razal, A.I. Minett, A new Raman metric for the characterisation of graphene oxide and its derivatives, *Sci. Rep.* 6 (2016) 1–6, <https://doi.org/10.1038/srep19491>.
- [39] A.C. Ferrari, Raman spectroscopy of graphene and graphite: disorder, electron-phonon coupling, doping and nonadiabatic effects, *Solid State Commun.* 143 (2007) 47–57, <https://doi.org/10.1016/j.ssc.2007.03.052>.
- [40] S. Reich, C. Thomsen, Raman spectroscopy of graphite, *Philos. Trans. R. Soc. London. Ser. A Math. Phys. Eng. Sci.* 362 (2004) 2271–2288, <https://doi.org/10.1098/rsta.2004.1454>.
- [41] P. Venezuela, M. Lazzari, F. Mauri, Theory of double-resonant Raman spectra in graphene: intensity and line shape of defect-induced and two-phonon bands, *Phys. Rev. B* 84 (2011), <https://doi.org/10.1103/PhysRevB.84.035433>, 035433.
- [42] A. Eckmann, A. Felten, A. Mishchenko, L. Britnell, R. Krupke, K.S. Novoselov, C. Casiraghi, Probing the nature of defects in graphene by Raman spectroscopy, *Nano Lett.* 12 (2012) 3925–3930, <https://doi.org/10.1021/nl300901a>.
- [43] C. Casiraghi, S. Pisana, K.S. Novoselov, A.K. Geim, A.C. Ferrari, Raman fingerprint of charged impurities in graphene, *Appl. Phys. Lett.* 91 (2007) 12–14, <https://doi.org/10.1063/1.2818692>.
- [44] S. Piscanec, M. Lazzari, F. Mauri, A.C. Ferrari, Optical phonons of graphene and nanotubes, *Eur. Phys. J. Spec. Top.* 148 (2007) 159–170, <https://doi.org/10.1140/epjst/e2007-00236-2>.
- [45] S. Ghosh, K. Ganesan, S.R. Polaki, T.R. Ravindran, N.G. Krishna, M. Kamruddin, A.K. Tyagi, Evolution and defect analysis of vertical graphene nanosheets, *J. Raman Spectrosc.* 45 (2014) 642–649, <https://doi.org/10.1002/jrs.4530>.
- [46] G. Gao, D. Liu, S. Tang, C. Huang, M. He, Y. Guo, X. Sun, B. Gao, Heat-initiated chemical functionalization of graphene, *Sci. Rep.* 6 (2016) 20034, <https://doi.org/10.1038/srep20034>.
- [47] J. Hwang, M. Kim, D. Campbell, H.A. Alsaman, J.Y. Kwak, S. Shivaraman, A.R. Woll, A.K. Singh, R.G. Hennig, S. Gorantla, M.H. Rummeli, M.G. Spencer, van der Waals epitaxial growth of graphene on sapphire by chemical vapor deposition without a metal catalyst, *ACS Nano* 7 (2013) 385–395, <https://doi.org/10.1021/nn305486x>.
- [48] P. Esquinazi, J. Krüger, J. Barzola-Quíquia, R. Schönemann, T. Herrmannsdörfer, N. García, On the low-field Hall coefficient of graphite,



- AIP Adv. 4 (2014), <https://doi.org/10.1063/1.4902099>.
- [49] O.V. Yazyev, Y.P. Chen, Polycrystalline graphene and other two-dimensional materials, *Nat. Nanotechnol.* 9 (2014) 755–767, <https://doi.org/10.1038/nnano.2014.166>.
- [50] L. Tapasztó, P. Nemes-Incze, G. Dobrik, K. Jae Yoo, C. Hwang, L.P. Biró, Mapping the electronic properties of individual graphene grain boundaries, *Appl. Phys. Lett.* 100 (2012), <https://doi.org/10.1063/1.3681375>.
- [51] J.C. Koepke, J.D. Wood, D. Estrada, Z.Y. Ong, K.T. He, E. Pop, J.W. Lyding, Atomic-scale evidence for potential barriers and strong carrier scattering at graphene grain boundaries: a scanning tunneling microscopy study, *ACS Nano* 7 (2013) 75–86, <https://doi.org/10.1021/nn302064p>.
- [52] J. Yin, S. Slizovskiy, Y. Cao, S. Hu, Y. Yang, I. Lobanova, B.A. Piot, S.K. Son, S. Ozdemir, T. Taniguchi, K. Watanabe, K.S. Novoselov, F. Guinea, A.K. Geim, V. Fal'ko, A. Mishchenko, Dimensional reduction, quantum Hall effect and layer parity in graphite films, *Nat. Phys.* 15 (2019) 437–442, <https://doi.org/10.1038/s41567-019-0427-6>.
- [53] B.R. Matis, J.S. Burgess, F.A. Bulat, A.L. Friedman, B.H. Houston, J.W. Baldwin, Surface doping and band gap tunability in hydrogenated graphene, *ACS Nano* 6 (2012) 17–22, <https://doi.org/10.1021/nn2034555>.
- [54] G. Hong, Y. Han, T.M. Schutzius, Y. Wang, Y. Pan, M. Hu, J. Jie, C.S. Sharma, U. Müller, D. Poulikakos, On the mechanism of hydrophilicity of graphene, *Nano Lett.* 16 (2016) 4447–4453, <https://doi.org/10.1021/acs.nanolett.6b01594>.
- [55] C. Jang, S. Adam, J.-H. Chen, E.D. Williams, S. Das Sarma, M.S. Fuhrer, Tuning the effective fine structure constant in graphene: opposing effects of dielectric screening on short- and long-range potential scattering, *Phys. Rev. Lett.* 101 (2008) 146805, <https://doi.org/10.1103/PhysRevLett.101.146805>.
- [56] Y. Fan, W. Jiang, A. Kawasaki, Highly conductive few-layer graphene/Al<sub>2</sub>O<sub>3</sub> nanocomposites with tunable charge carrier type, *Adv. Funct. Mater.* 22 (2012) 3882–3889, <https://doi.org/10.1002/adfm.201200632>.
- [57] R. Song, W. Feng, C.A. Jimenez-Cruz, B. Wang, W. Jiang, Z. Wang, R. Zhou, Water film inside graphene nanosheets: electron transfer reversal between water and graphene via tight nano-confinement, *RSC Adv.* 5 (2015) 274–280, <https://doi.org/10.1039/C4RA13736A>.
- [58] T. Ohta, A. Bostwick, J.L. McChesney, T. Seyller, K. Horn, E. Rotenberg, Inter-layer interaction and electronic screening in multilayer graphene investigated with angle-resolved photoemission spectroscopy, *Phys. Rev. Lett.* 98 (2007) 16–19, <https://doi.org/10.1103/PhysRevLett.98.206802>.
- [59] W. Zhu, V. Perebeinos, M. Freitag, P. Avouris, Carrier scattering, mobilities, and electrostatic potential in monolayer, bilayer, and trilayer graphene, *Phys. Rev. B* 80 (2009) 235402, <https://doi.org/10.1103/PhysRevB.80.235402>.
- [60] F. Guinea, Charge distribution and screening in layered graphene systems, *Phys. Rev. B Condens. Matter* 75 (2007) 1–7, <https://doi.org/10.1103/PhysRevB.75.235433>.
- [61] E.H. Hwang, S. Das Sarma, Acoustic phonon scattering limited carrier mobility in two-dimensional extrinsic graphene, *Phys. Rev. B Condens. Matter* 77 (2008) 1–6, <https://doi.org/10.1103/PhysRevB.77.115449>.
- [62] V.M. Samoilov, E.A. Danilov, A.V. Nikolaeva, D.V. Ponomareva, I.A. Porodzinskii, E.R. Razyapov, I.A. Sharonov, N.A. Yashtulov, Electrical conductivity of a carbon reinforced alumina resistive composite material based on synthetic graphite and graphene, *Inorg. Mater.* 54 (2018) 601–609, <https://doi.org/10.1134/s0020168518060110>.
- [63] G. Yamamoto, M. Omori, T. Hashida, H. Kimura, A novel structure for carbon nanotube reinforced alumina composites with improved mechanical properties, *Nanotechnology* 19 (2008), <https://doi.org/10.1088/0957-4484/19/31/315708>.
- [64] Q. Yuchang, W. Qinlong, L. Fa, Z. Wancheng, Temperature dependence of the electromagnetic properties of graphene nanosheet reinforced alumina ceramics in the X-band, *J. Mater. Chem. C* 4 (2016) 4853–4862, <https://doi.org/10.1039/C6TC01163B>.
- [65] C. Ramirez, F.M. Figueiredo, P. Miranzo, P. Poza, M.I. Osendi, Graphene nanoplatelet/silicon nitride composites with high electrical conductivity, *Carbon* N. Y. 50 (2012) 3607–3615, <https://doi.org/10.1016/j.carbon.2012.03.031>.
- [66] S. Stankovich, D.A. Dikin, G.H.B. Dommett, K.M. Kohlhaas, E.J. Zimney, E.A. Stach, R.D. Piner, S.T. Nguyen, R.S. Ruoff, Graphene-based composite materials, *Nature* 442 (2006) 282–286, <https://doi.org/10.1038/nature04969>.